



Cite this: *Mater. Adv.*, 2023,  
4, 1566

# The electronic and interfacial properties of a vdW heterostructure composed of penta-PdSe<sub>2</sub> and biphenylene monolayers

Muhammad Azhar Nazir, Yiheng Shen, Arzoo Hassan  and Qian Wang \*

It is of current interest to develop van der Waals (vdW) heterostructures with tunable electronic properties for technical applications. Motivated by the synthesis of a metallic carbon nanosheet termed the biphenylene network (BPN) [Q. Fan, L. Yan, M. W. Tripp, O. Krejčí, S. Dimosthenous, S. R. Kachel, M. Chen, A. S. Foster, U. Koert, P. Liljeroth *et al.*, *Science*, 2021, **372**, 852–856] and semiconducting penta-PdSe<sub>2</sub> sheets [A. D. Oyedele, S. Yang, L. Liang, A. A. Puzetzyk, K. Wang, J. Zhang, P. Yu, P. R. Pudasaini, A. W. Ghosh, Z. Liu *et al.*, *J. Am. Chem. Soc.*, 2017, **139**, 14090–14097], we rationally design a vdW heterostructure by vertically stacking these two individual sheets. The state-of-the-art first-principles calculations show that the penta-PdSe<sub>2</sub> sheet well preserves its intrinsic properties when forming a vdW contact with BPN. The heterostructure possesses an n-type Schottky contact with a Schottky barrier of 0.54 eV, and a negative band-bending of 0.56 eV at the lateral interface with electrons as major transport carriers. These features make the penta-PdSe<sub>2</sub>/BPN heterojunction promising for applications in field-effect transistors.

Received 7th February 2023,  
Accepted 10th February 2023

DOI: 10.1039/d3ma00064h

rsc.li/materials-advances

## 1. Introduction

The assembly of different two-dimensional (2D) materials into vertically stacked van der Waals (vdW) heterostructures has fueled a novel concept of designing and synthesizing new materials with improved functionalities distinct from those of each component.<sup>1–3</sup> Unlike traditional heterostructures, which strongly rely on direct covalent bonding and strict lattice-matching conditions,<sup>4</sup> the weak vdW interaction and the absence of covalent bonding between the two components allow the construction of an artificial interface that offers a great degree of freedom for interlayer engineering. More importantly, the absence of dangling bonds endows 2D materials with great potential and excellent stacking stability to construct vdW heterostructures in an arbitrary sequence.<sup>5</sup> Since the discovery of graphene,<sup>6</sup> significant efforts have been devoted to the design of vdW heterostructures by stacking various 2D sheets, including graphene,<sup>7,8</sup> penta-graphene,<sup>9,10</sup> graphitic carbon nitride,<sup>11,12</sup> transition metal-carbides,<sup>13,14</sup> and boron nitrides,<sup>15,16</sup> for their potential applications in the fields like energy storage,<sup>17–19</sup> photocatalysis,<sup>20,21</sup> and optoelectronic devices.<sup>22–24</sup> It is also worth mentioning that extensive research is still underway to design and synthesize vdW heterostructures with desired properties under various conditions.

In parallel to the design and synthesis of new heterostructures constructed using hexagonal building blocks, geometrically assembled vdW heterostructures have become the major research hotspot for realizing more controllable devices. Considering the structure–property relationship, one can expect that vdW heterostructures composed of layers with different geometrical configurations would exhibit different properties. In this regard, pentagonal materials have initiated a new era in materials with the prediction of penta-graphene<sup>25,26</sup> and the synthesis of penta-PdSe<sub>2</sub>,<sup>27</sup> penta-NiN<sub>2</sub>,<sup>28</sup> and penta-Si nanoribbons<sup>29</sup> as practical templates to construct pentagon-based vdW heterostructures. Additionally, their uniqueness in device functions strongly depends on their underlying electronic structures and pentagonal stacking patterns to tune the structure–property relationship. Among these, the PdSe<sub>2</sub> sheet has attracted increasing research interest due to its excellent performance in electronics. For example, a high electron field-effect mobility of  $\sim 158 \text{ cm}^2 \text{ V}^{-1} \text{ s}^{-1}$  in few-layer PdSe<sub>2</sub> extends its credibility in field-effect transistors (FETs).<sup>27</sup> From the device's perspective, a large rectification ratio of up to  $6.3 \times 10^5$  for PdSe<sub>2</sub>/MoTe<sub>2</sub>,<sup>30</sup>  $5.5 \times 10^5$  for PdSe<sub>2</sub>/GeSe,<sup>31</sup> a high photoresponsivity of  $58.8 \text{ A W}^{-1}$  (at 1650 nm) for PdSe<sub>2</sub>/InSe,<sup>32</sup>  $6.9 \text{ A W}^{-1}$  for PdSe<sub>2</sub>/MoS<sub>2</sub>,<sup>33</sup> a high specific detectivity of  $5.29 \times 10^{11}$  Jones for PdSe<sub>2</sub>/MoSe<sub>2</sub>,<sup>34</sup> and significant broadband image sensing for PdSe<sub>2</sub>/MoTe<sub>2</sub>,<sup>35</sup> PdSe<sub>2</sub>/WS<sub>2</sub><sup>36</sup> vdW heterostructures extend the contact realization of PdSe<sub>2</sub> sheets under applied conditions. In addition to the experimental results, Hassan

School of Materials Science and Engineering, Peking University, Beijing 100871, China. E-mail: qianwang2@pku.edu.cn



*et al.*<sup>37</sup> and Li *et al.*<sup>38</sup> investigated the interfacial properties of PdSe<sub>2</sub>-graphene and PdSe<sub>2</sub>-metal contacts under different conditions. These advances clearly show that the penta-PdSe<sub>2</sub> sheet can flexibly form heterojunctions with other 2D materials.

Recently, Fan *et al.*<sup>39</sup> synthesized an ultra-flat metallic carbon sheet, namely the biphenylene network (BPN), which is composed of tetra-, hexa-, and octa-gonal rings and features pure sp<sup>2</sup>-hybridization. By using first-principles calculations, some theoretical studies have also confirmed metallicity,<sup>40</sup> magnetic and topological ordering,<sup>41</sup> anisotropic charge transport,<sup>42</sup> and remarkable negative thermal expansion<sup>43</sup> in the BPN monolayer, which extend the functionality of this sheet for advanced nanodevices. From the perspective of heterojunctions, it would be interesting to explore how the BPN sheet interacts with penta-PdSe<sub>2</sub> to form a heterostructure.

In this work, we report the first study on the electronic and interfacial properties of a 2D vdW heterostructure composed of vertically stacked penta-PdSe<sub>2</sub> and BPN monolayers. We demonstrate that the heterostructure exhibits an n-type Schottky contact feature as well as negative band-bending at the lateral interface of the heterojunction, suggesting that the PdSe<sub>2</sub>/BPN heterostructure is promising for FET devices.

## 2. Computational details

All the calculations are performed within the framework of density functional theory (DFT) implemented in Vienna *ab initio* Simulation Package (VASP).<sup>44,45</sup> The projector-augmented-wave (PAW) method is used to describe the interactions between valence electrons and ion cores.<sup>46</sup> The generalized gradient approximation (GGA)<sup>47</sup> based Perdew–Burke–Ernzerhof (PBE) functional is used to treat the electronic exchange–correlation interactions of electrons.<sup>46</sup> In addition, the DFT-D3 functional<sup>48,49</sup> is considered for all the calculations to describe the effect of vdW interactions in the PdSe<sub>2</sub>/BPN heterostructure. The valence electronic configurations of 5s<sup>1</sup>4d<sup>9</sup>, 4s<sup>2</sup>4p<sup>4</sup>, and 2s<sup>2</sup>2p<sup>2</sup> are taken for Pd, Se, and C atoms, respectively. The kinetic energy cut-off of 520 eV is used to expand the wave functions and pseudo-atomic calculations. A vacuum space of 25 Å along the z-direction (perpendicular to the PdSe<sub>2</sub>/BPN heterojunction layers) separates the contact regions to prevent interactions between the periodic images. The first Brillouin zone (BZ) is sampled with a fine grid of 9 × 2 × 1. The atomic positions are fully relaxed with an energy convergence threshold of 10<sup>−4</sup> eV and a force convergence threshold of 0.01 eV Å<sup>−1</sup>. *Ab initio* molecular dynamics (AIMD) simulations are performed under the canonical ensemble, and the temperature fluctuation is controlled by the Nosé–Hoover thermostat.<sup>50</sup>

## 3. Results and discussion

### 3.1. Structure and electronic properties of free-standing PdSe<sub>2</sub> and BPN monolayers

Before focusing on the PdSe<sub>2</sub>/BPN heterojunction, we first discuss the geometric structure and electronic properties of the free-standing PdSe<sub>2</sub> and BPN monolayers, as shown in Fig. 1. The

lattice of the penta-PdSe<sub>2</sub> monolayer belongs to the monoclinic *P21/C* symmetry (space group no. 14), with the optimized lattice constants of *a* = 5.75 Å and *b* = 5.92 Å, whereas the BPN layer possesses an orthorhombic *Pmma* symmetry (space group no. 47), with the optimized constants of *a* = 3.76 Å and *b* = 4.52 Å. Studies reveal that both individual sheets well preserve their environmental potential by offering dynamical, thermal and mechanical stability under applied conditions.<sup>27,39,40,51</sup> The electronic band structures illustrate that penta-PdSe<sub>2</sub> is semiconducting with an indirect band gap of 1.36 eV, while the BPN monolayer is metallic because the partially filled energy bands cross the Fermi level. Furthermore, the partial density of states (PDOS) of the PdSe<sub>2</sub> sheet shows that the valence band maximum (VBM) and conduction band minimum (CBM) are mainly contributed by the Pd-4d and Se-4p orbitals.

### 3.2. Structure and stability of the PdSe<sub>2</sub>/BPN heterostructure

We design the PdSe<sub>2</sub>/BPN heterostructure by vertically stacking the two monolayers. Unlike the heterostructures purely composed of hexagonal building blocks,<sup>15,52–55</sup> the PdSe<sub>2</sub>/BPN heterojunction comprises mixed geometric blocks such as tetra-hexa and octagonal blocks of C as well as purely pentagonal blocks composed of Pd and Se atoms. Due to the different lattice symmetries and lattice parameters, special attention is devoted to control the lattice mismatch between the penta-PdSe<sub>2</sub> and BPN layers in order to do calculations using periodic boundary conditions. In this respect, we used a cell-matching code<sup>56</sup> to construct PdSe<sub>2</sub>/BPN supercells, which are very suitable for making a vdW interface between two 2D sheets with different lattice constants and symmetrical images by controlling a minimal strain in the stacked supercell. Particularly, in this method, one sheet is placed on the other, and the most suitable shape of the stacked supercell is calculated by rotating that sheet by an angle ranging from 0 to 90° with a step difference of 1°. For PdSe<sub>2</sub>/BPN, we found the best match of the stacked configurations at 38° with the minimum number of atoms (60 C atoms, 20 Se atoms, and 10 Pd atoms) and the lattice mismatch threshold of 1%, as shown in Fig. 2(a). To save the computational cost, this configuration is considered for further investigations.

The optimized distance between the vertically stacked PdSe<sub>2</sub> and BPN layers is 3.40 Å. To examine the interface stability of this system, we calculate its binding energy *E<sub>b</sub>* with the following equation  $E_b = -[(E_H - E_x - E_y)/A]$ , where *E<sub>H</sub>* is the total energy of the PdSe<sub>2</sub>/BPN heterostructure, *E<sub>x</sub>* and *E<sub>y</sub>* are the total energies of the free-standing penta-PdSe<sub>2</sub> and BPN monolayers, respectively, and *A* is the total area of the supercell of the heterostructure. The calculated binding energy *E<sub>b</sub>* is 0.06 eV Å<sup>−2</sup>. The values of interlayer distance *d* and binding energy are comparable with those of the typical vdW crystals such as graphite [*E<sub>b</sub>* = 0.28 J m<sup>−2</sup> (0.0175 eV Å<sup>−2</sup>) and *d* = 3.60 Å]<sup>57</sup> and hexagonal BN (*E<sub>b</sub>* = 0.04 eV Å<sup>−2</sup> and *d* = 3.30 Å),<sup>58</sup> and some recently reported vdW heterostructures such as PdSe<sub>2</sub>/graphene (*E<sub>b</sub>* = 0.02 eV Å<sup>−2</sup> and *d* = 3.60 Å),<sup>37</sup> implying that the PdSe<sub>2</sub>/BPN heterostructure can be classified based on the category of vdW type.



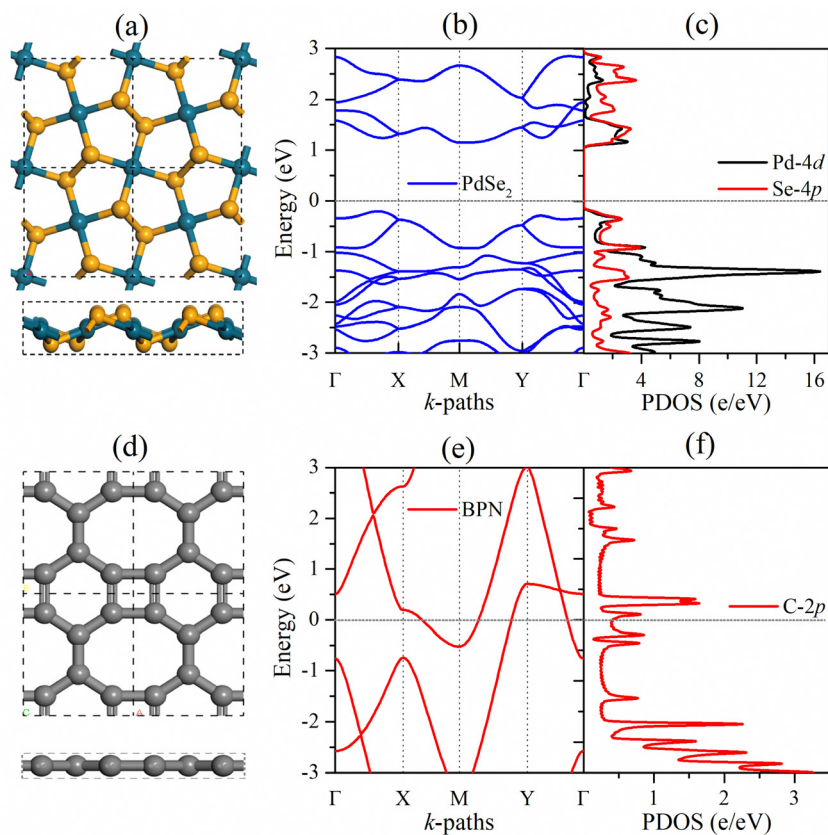


Fig. 1 Top and side views of  $2 \times 2$ , electronic band structure, and the corresponding PDOS of the free-standing (a)–(c) penta-PdSe<sub>2</sub>, and (d)–(f) BPN monolayer. The Fermi energy ( $E_F$ ) is set to 0 eV. The cyan, yellow, and grey spheres represent Pd, Se, and C atoms, respectively.

Furthermore, the thermal stability of the PdSe<sub>2</sub>/BPN system is investigated at 500 K with an AIMD simulation. The fluctuation of the total potential energy during a simulation time of 10 picoseconds (ps) with a time step of 1 femtosecond (fs) is plotted in Fig. 2(b). One can see that after 10 000 steps, there is still no significant geometric distortion, and the energy of this system vibrates around a constant, confirming that the PdSe<sub>2</sub>/BPN heterostructure is thermally stable at 500 K.

### 3.3. Interfacial properties of the PdSe<sub>2</sub>/BPN heterostructure

The vdW interactions between the stacked monolayers can provide more freedom to engineer the carrier injections from a highly conductive electrode to a semiconductor channel for designing high-performance electronic devices. In order to analyze the electronic properties of the PdSe<sub>2</sub>/BPN system, we calculate the electronic band structure of the heterostructure and its projection on the PdSe<sub>2</sub> and BPN sheets. As shown in

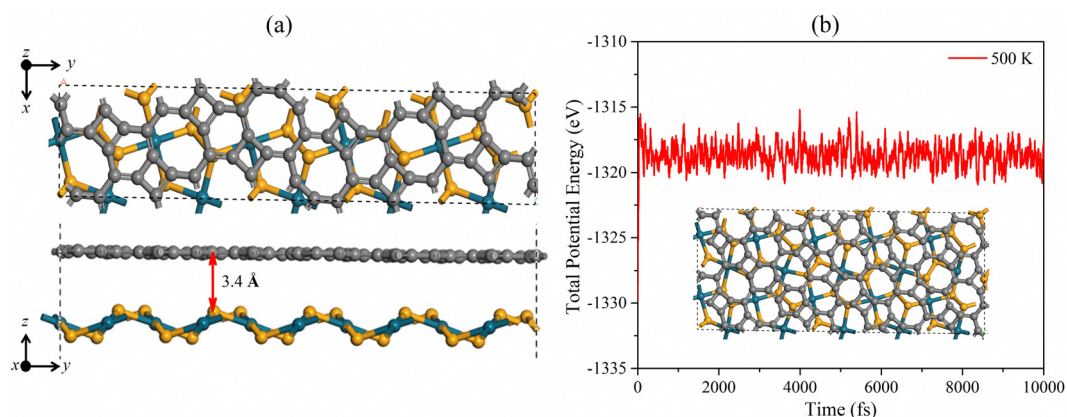


Fig. 2 (a) Top and side views of  $1 \times 1$ , and (b) total potential energy fluctuation of the PdSe<sub>2</sub>/BPN heterostructure at 500 K.





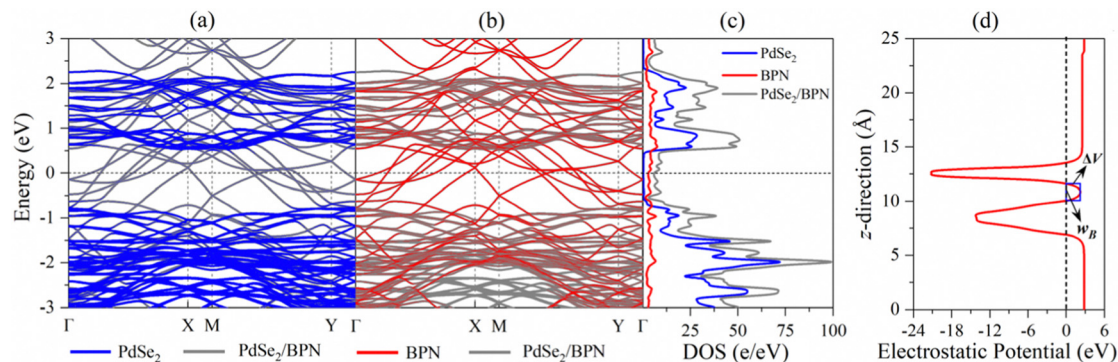


Fig. 3 Projected band structures of (a) PdSe<sub>2</sub> and (b) BPN monolayers where the grey lines represent the band structure of the PdSe<sub>2</sub>/BPN heterostructure. (c) DOS of penta-PdSe<sub>2</sub>, BPN, and the PdSe<sub>2</sub>/BPN heterostructure. (d) Electrostatic potential profile of the PdSe<sub>2</sub>/BPN heterostructure along the z-direction. The rectangular blue box represents the tunneling barrier, where  $\Delta V$  and  $w_B$  are the tunneling barrier height and width, respectively.

Fig. 3(a) and (b), the electronic structures of both PdSe<sub>2</sub> and BPN monolayers are well preserved, further confirming that the PdSe<sub>2</sub>/BPN system is a vdW heterostructure. In addition, as shown in Fig. 3(c), the DOS of the PdSe<sub>2</sub>/BPN heterojunction around the Fermi level is mainly contributed by the BPN sheet.

We further explore the device performance of the PdSe<sub>2</sub>/BPN-based FET. As shown in the schematic in Fig. 4, the movement of charge carriers from the metallic electrode to the semiconducting channel needs to overcome three types of barriers, including the tunneling barrier, Schottky barrier ( $\Phi_V$ ), and lateral barrier ( $\Phi_L$ ). Among them, the tunneling barrier appears at the vertical interface B between the PdSe<sub>2</sub> and BPN sheets because of the quantum features of the carriers, which strongly depends on the interface between the metal and the semiconductor. The Schottky barrier also appears at the vertical interface B. The magnitude of the Schottky barrier between an electrode and channel materials mainly depends on the nature of the electrode material, work function, and contact resistance. Additionally, the lateral barrier exists at the lateral interface D between the heterostructure and the channel and can be estimated by the band bending ( $\Delta E_F$ ) values.

First, we evaluate the tunneling possibility (TP) of the PdSe<sub>2</sub>/BPN system from the tunneling barrier in the electrostatic potential profile, which is marked by the blue rectangle in Fig. 3(d), based on the Wentzel–Kramers–Brillouin (WKB) approximation,<sup>37</sup>

$$TP = \exp\left(-2\frac{\sqrt{2m\Delta V}}{\hbar} \times w_B\right) \quad (1)$$

where  $\Delta V$  and  $w_B$  represent the height and width of the tunneling barrier,  $m$  is the electron mass, and  $\hbar$  is the reduced Planck's constant. The calculated TP of the PdSe<sub>2</sub>/BPN system is 60%, which is higher than that of many PdSe<sub>2</sub>/metal contacts, including PdSe<sub>2</sub>/Ag, PdSe<sub>2</sub>/Au, and PdSe<sub>2</sub>/Pb, while it is lower than that of the PdSe<sub>2</sub>/Cu and PdSe<sub>2</sub>/Ti contacts.<sup>37</sup> Detailed information is enlisted in Table 1. The relatively high TP of the PdSe<sub>2</sub>/BPN heterostructure extends its suitability for high-performance FETs. In addition, the PdSe<sub>2</sub>/BPN heterostructure possesses a 60% lower tunneling barrier height as compared to that of the PdSe<sub>2</sub>/graphene system, indicating that its TP could be larger than that of the PdSe<sub>2</sub>/graphene contact, because a low tunneling barrier leads to high TP according to the WKB approximation.

Next, we calculate the Schottky barrier of the PdSe<sub>2</sub>/BPN heterostructure, which is among the most important parameters to determine the contact resistance in a FET device. Following the Schottky–Mott rule,<sup>37</sup> the Schottky barrier height (SBH) of electrons ( $\Phi_e$ ) and holes ( $\Phi_h$ ) is defined as the energy difference between the Fermi level and the respective energy band edges of the semiconductor,

$$\Phi_e = E_{CBM} - E_F, \quad \Phi_h = E_F - E_{VBM} \quad (2)$$

where  $E_F$  represents the Fermi level, while  $E_{CBM}$  and  $E_{VBM}$  are the band edges of PdSe<sub>2</sub> identified from the projected band structure. For device applications, a small SBH is desired for low contact resistance. From eqn (2), we obtain an SBH value of 0.54 eV for electrons and 0.80 eV for holes in the PdSe<sub>2</sub>/BPN heterostructure. This inspection uncovers that the Fermi level

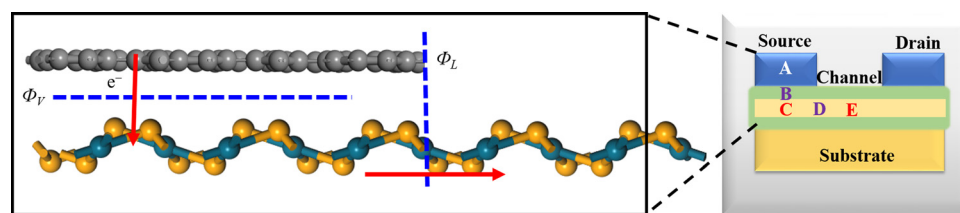


Fig. 4 A typical illustration of the FET three regions (A), (C), and (E) with two interfaces (B) and (D). Movement of the charge carriers from the metallic electrode BPN to the semiconducting penta-PdSe<sub>2</sub> channel, where  $\Phi_V$  and  $\Phi_L$  represent the Schottky barrier and lateral barrier, respectively.



**Table 1** Calculated parameters of PdSe<sub>2</sub>-based heterostructures, including the interlayer distance  $d$  (in Å), the binding energy  $E_b$  (in eV Å<sup>-2</sup>), the tunneling barrier height  $\Delta V$  (in eV), width  $w_B$  (in Å), the tunneling possibility  $T_p$  (in %), the work function  $W_H$  (eV) for heterostructures, the Schottky barriers  $\Phi_e$  and  $\Phi_h$  (in eV), and the band-bending  $\Delta E_F$  (in eV)

Structure	$d$	$E_b$	$\Delta V$	$w_B$	TP	$W_H$	$\Phi_e$	$\Phi_h$	$\Delta E_F$
PdSe <sub>2</sub> /BPN	3.4	0.06	1.5	2.3	60	4.64	0.54	0.80	-0.56
PdSe <sub>2</sub> /graphene <sup>37</sup>	3.6	0.02	3.8	—	—	—	0.22	—	-0.94
PdSe <sub>2</sub> /Ag <sup>37</sup>	2.9	0.38	4.0	17.7	40	4.43	0.87	0.56	0.05
PdSe <sub>2</sub> /Au <sup>37</sup>	2.9	0.44	3.2	10.4	18	5.24	0.62	0.81	0.03
PdSe <sub>2</sub> /Cu <sup>37</sup>	2.5	0.57	0.0	0.0	100	4.49	0.79	0.64	-0.51
PdSe <sub>2</sub> /Ti <sup>37</sup>	2.5	1.34	0.0	0.0	100	5.20	0.58	0.85	-0.14
PdSe <sub>2</sub> /Pb <sup>37</sup>	3.1	0.31	2.4	9.2	9.2	4.11	0.76	0.67	0.41
PdSe <sub>2</sub> /Sc <sup>38</sup>	2.1	—	—	—	—	3.5	—	—	—
PdSe <sub>2</sub> /Al <sup>38</sup>	2.3	—	—	—	—	4.3	0.12	—	—
PdSe <sub>2</sub> /MoTe <sub>2</sub> <sup>38</sup>	3.2	—	—	—	—	5.19	—	—	—

is closer to the CBM of the PdSe<sub>2</sub> sheet in the heterostructure, indicating an n-type Schottky contact in the PdSe<sub>2</sub>/BPN system with electrons as the major transport carriers, which was previously reported for PdSe<sub>2</sub>/graphene, PdSe<sub>2</sub>/Ti and PdSe<sub>2</sub>/Au contacts.<sup>37</sup> Besides, the SBH for the major carrier is lower than that of most PdSe<sub>2</sub>/metal contacts,<sup>37</sup> as shown in Table 1, which is preferred for FET applications. In particular, it is lower than the SBH of the PdSe<sub>2</sub>/Cu and PdSe<sub>2</sub>/Ti contacts with high TP.

In addition, to estimate the lateral barrier, we study the band bending in PdSe<sub>2</sub>/BPN heterostructures in the scheme of the current-in-plane (CIP)<sup>9</sup> model. As shown in Fig. 5, the CIP model is mainly divided into three parts: the left side for the PdSe<sub>2</sub>/BPN heterojunction, the middle one for the interface between the heterojunction and the free-standing monolayer, and the right side for the free-standing PdSe<sub>2</sub> layer. The energy levels for the heterojunction and the free-standing PdSe<sub>2</sub> layer are aligned to the vacuum energy ( $E_{vac}$ ). The work functions of

the PdSe<sub>2</sub>/BPN heterojunction and the free-standing PdSe<sub>2</sub> monolayer are calculated to be  $W_H = 4.64$  eV and  $W_{PdSe_2} = 5.20$  eV, respectively. As listed in Table 1, the band bending  $\Delta E_F$  at the lateral interface D is estimated by  $\Delta E_F = W_H - W_{PdSe_2} = -0.56$  eV, which is quite comparable to the vdW contacts such as PdSe<sub>2</sub>/graphene and PdSe<sub>2</sub>/Ti with  $\Delta E_F = -0.94$  and  $-0.14$  eV, respectively.<sup>37</sup> The negative band bending ( $\Delta E_F < 0$ ) confirms that an n-type channel is formed between the PdSe<sub>2</sub>/BPN heterostructure and the free-standing PdSe<sub>2</sub> sheet, as reported in PdSe<sub>2</sub>/graphene<sup>37</sup> and PdSe<sub>2</sub>/Al contacts.<sup>38</sup>

Due to its relatively high TP and low SBH, the contact between PdSe<sub>2</sub> and BPN could be among the most suitable design for PdSe<sub>2</sub>-based FET applications.

## 4. Conclusions

In this work, we report a vdW heterostructure composed of purely pentagonal PdSe<sub>2</sub> and atomically flat carbon allotrope BPN, which serve as the channel and electrode materials, respectively, because of their intrinsic semiconducting and metallic features. The energetic and thermal stabilities of this heterostructure are confirmed by the binding energy calculations and AIMD simulations. The heterostructure possesses an n-type Schottky contact and negative band-bending at the lateral interface with electrons as major transport carriers. Compared to the vdW heterostructure of penta-PdSe<sub>2</sub>/graphene, the penta-PdSe<sub>2</sub>/BPN heterojunction has a lower tunneling barrier height due to the co-existence of 4- and 8-rings in the BPN sheet, leading to a high tunneling possibility of ~60% at the junction. Together with the synthesis of PdSe<sub>2</sub> and BPN sheets, these findings would trigger more explorations for the PdSe<sub>2</sub>/BPN heterostructure in future device applications.

## Conflicts of interest

The authors declare that they have no competing financial interests or personal relationships that could have appeared to influence the work reported in this paper.

## Acknowledgements

This work is partially supported by grants from the National Natural Science Foundation of China (Grant no. NSFC-11974028 and NSFC-12274007) and the National Key Research and Development Program of the Ministry of Science and Technology of the People's Republic of China (2017YFA0205003). This work is also supported by the high-performance computing platform of Peking University, China.

## References

- W. Liao, Y. Huang, H. Wang and H. Zhang, *Appl. Mater. Today*, 2019, **16**, 435–455.

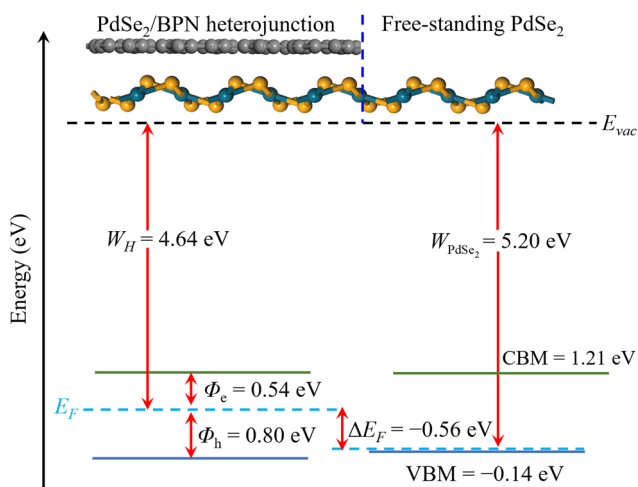


**Fig. 5** Schematic diagram of the CIP model and band alignment in the PdSe<sub>2</sub>/BPN heterojunction.  $E_{vac}$  is the vacuum level to align all the values, and  $W_H$  and  $W_{PdSe_2}$  are the work functions of the PdSe<sub>2</sub>/BPN heterostructure and free-standing PdSe<sub>2</sub> monolayer. The blue, black, and cyan dashed lines represent the interface between the electrode and channel regions, vacuum level, and the Fermi energy, respectively. The green and blue solid lines indicate the CBM and VBM values.



- 2 K. Novoselov, A. Mishchenko, A. Carvalho and A. Castro Neto, *Science*, 2016, **353**, aac9439.
- 3 A. K. Geim and I. V. Grigorieva, *Nature*, 2013, **499**, 419–425.
- 4 P. Wang, C. Jia, Y. Huang and X. Duan, *Matter*, 2021, **4**, 552–581.
- 5 Y. Wang, J. Pang, Q. Cheng, L. Han, Y. Li, X. Meng, B. Ibarlucea, H. Zhao, F. Yang and H. Liu, *Nano-Micro Lett.*, 2021, **13**, 1–52.
- 6 K. S. Novoselov, A. K. Geim, S. V. Morozov, D.-E. Jiang, Y. Zhang, S. V. Dubonos, I. V. Grigorieva and A. A. Firsov, *Science*, 2004, **306**, 666–669.
- 7 Z. Zhang, P. Lin, Q. Liao, Z. Kang, H. Si and Y. Zhang, *Adv. Mater.*, 2019, **31**, 1806411.
- 8 X. Wu, R. Yang, X. Chen and W. Liu, *Nanomaterials*, 2022, **12**, 196.
- 9 Y. Guo, F. Q. Wang and Q. Wang, *Appl. Phys. Lett.*, 2017, **111**, 073503.
- 10 A. Hassan, Y. Guo, Q. Wang, Y. Kawazoe and P. Jena, *J. Appl. Phys.*, 2019, **125**, 065308.
- 11 G.-C. Guo, R.-Z. Wang, B.-M. Ming, C. Wang, S.-W. Luo, M. Zhang and H. Yan, *J. Mater. Chem. A*, 2019, **7**, 2106–2113.
- 12 J. Fu, J. Yu, C. Jiang and B. Cheng, *Adv. Energy Mater.*, 2018, **8**, 1701503.
- 13 Z. Kou, T. Wang, Q. Gu, M. Xiong, L. Zheng, X. Li, Z. Pan, H. Chen, F. Verpoort and A. K. Cheetham, *Adv. Energy Mater.*, 2019, **9**, 1803768.
- 14 J. Zhu, H. Wang, L. Ma and G. Zou, *Nano Res.*, 2021, **14**, 3416–3422.
- 15 X. Song, J. Sun, Y. Qi, T. Gao, Y. Zhang and Z. Liu, *Adv. Energy Mater.*, 2016, **6**, 1600541.
- 16 S. Ullah, P. A. Denis, M. G. Menezes and F. Sato, *Comput. Mater. Sci.*, 2021, **188**, 110233.
- 17 D. K. Bediako, M. Rezaee, H. Yoo, D. T. Larson, S. Zhao, T. Taniguchi, K. Watanabe, T. L. Brower-Thomas, E. Kaxiras and P. Kim, *Nature*, 2018, **558**, 425–429.
- 18 P. Das, Q. Fu, X. Bao and Z.-S. Wu, *J. Mater. Chem. A*, 2018, **6**, 21747–21784.
- 19 E. Pomerantseva and Y. Gogotsi, *Nat. Energy*, 2017, **2**, 1–6.
- 20 Y.-L. Liu, Y. Shi, H. Yin and C.-L. Yang, *Appl. Phys. Lett.*, 2020, **117**, 063901.
- 21 K. Ren, J. Yu and W. Tang, *J. Alloys Compd.*, 2020, **812**, 152049.
- 22 J. Y. Lee, J.-H. Shin, G.-H. Lee and C.-H. Lee, *Nanomaterials*, 2016, **6**, 193.
- 23 A. Abid, M. Haneef, S. Ali and A. Dahshan, *J. Phys. Chem. Solids*, 2022, **161**, 110433.
- 24 S. J. Liang, B. Cheng, X. Cui and F. Miao, *Adv. Mater.*, 2020, **32**, 1903800.
- 25 S. Zhang, J. Zhou, Q. Wang, X. Chen, Y. Kawazoe and P. Jena, *Proc. Natl. Acad. Sci. U. S. A.*, 2015, **112**, 2372–2377.
- 26 M. A. Nazir, A. Hassan, Y. Shen and Q. Wang, *Nano Today*, 2022, **44**, 101501.
- 27 A. D. Oyedele, S. Yang, L. Liang, A. A. Puzos, K. Wang, J. Zhang, P. Yu, P. R. Pudasaini, A. W. Ghosh and Z. Liu, *et al.*, *J. Am. Chem. Soc.*, 2017, **139**, 14090–14097.
- 28 M. Bykov, E. Bykova, A. V. Ponomareva, F. Tasnadi, S. Chariton, V. B. Prakapenka, K. Glazyrin, J. S. Smith, M. F. Mahmood and I. A. Abrikosov, *ACS Nano*, 2021, **15**, 13539–13546.
- 29 J. I. Cerdá, J. Sławińska, G. Le Lay, A. C. Marele, J. M. Gómez-Rodríguez and M. E. Dávila, *Nat. Commun.*, 2016, **7**, 1–7.
- 30 A. M. Afzal, M. Z. Iqbal, G. Dastgeer, A. U. Ahmad and B. Park, *Adv. Sci.*, 2021, **8**, 2003713.
- 31 A. M. Afzal, M. Z. Iqbal, S. Mumtaz and I. Akhtar, *J. Mater. Chem. C*, 2020, **8**, 4743–4753.
- 32 W. Ahmad, J. Liu, J. Jiang, Q. Hao, D. Wu, Y. Ke, H. Gan, V. Laxmi, Z. Ouyang and F. Ouyang, *Adv. Funct. Mater.*, 2021, **31**, 2104143.
- 33 H. Gao, C. Du, L. Chen, W. Wang and K. Li, *Adv. Mater. Interfaces*, 2022, **9**, 2102350.
- 34 J. Zhong, B. Wu, Y. Madoune, Y. Wang, Z. Liu and Y. Liu, *Nano Res.*, 2022, **15**, 2489–2496.
- 35 L. Pi, P. Wang, S.-J. Liang, P. Luo, H. Wang, D. Li, Z. Li, P. Chen, X. Zhou and F. Miao, *Nat. Electron.*, 2022, **5**, 248–254.
- 36 X. Kang, C. Lan, F. Li, W. Wang, S. Yip, Y. Meng, F. Wang, Z. Lai, C. Liu and J. C. Ho, *Adv. Opt. Mater.*, 2021, **9**, 2001991.
- 37 A. Hassan, Y. Guo and Q. Wang, *ACS Appl. Electron. Mater.*, 2020, **2**, 2535–2542.
- 38 P. Li, W. Qi and K. Tang, *Chin. J. Phys.*, 2022, **78**, 57–71.
- 39 Q. Fan, L. Yan, M. W. Tripp, O. Krejčí, S. Dimosthenous, S. R. Kachel, M. Chen, A. S. Foster, U. Koert and P. Liljeroth, *et al.*, *Science*, 2021, **372**, 852–856.
- 40 A. Bafekry, M. Faraji, M. Fadlallah, H. Jappor, S. Karbasizadeh, M. Ghergherehchi and D. Gogova, *J. Phys.: Condens. Matter*, 2021, **34**, 015001.
- 41 Y.-W. Son, H. Jin and S. Kim, *Nano Lett.*, 2022, **22**, 3112–3117.
- 42 I. Alcón, G. Calogero, N. Papior, A. Antidormi, K. Song, A. W. Cummings, M. Brandbyge and S. Roche, *J. Am. Chem. Soc.*, 2022, **144**, 8278–8285.
- 43 Q. Li, J. Zhou, G. Liu and X. Wan, *Carbon*, 2022, **187**, 349–353.
- 44 G. Kresse and J. Furthmüller, *Phys. Rev. B: Condens. Matter Mater. Phys.*, 1996, **54**, 11169.
- 45 G. Kresse and D. Joubert, *Phys. Rev. B: Condens. Matter Mater. Phys.*, 1999, **59**, 1758.
- 46 P. E. Blöchl, *Phys. Rev. B: Condens. Matter Mater. Phys.*, 1994, **50**, 17953.
- 47 J. P. Perdew, K. Burke and M. Ernzerhof, *Phys. Rev. Lett.*, 1996, **77**, 3865.
- 48 J. Klimeš, D. R. Bowler and A. Michaelides, *J. Phys.: Condens. Matter*, 2009, **22**, 022201.
- 49 J. Klimeš, D. R. Bowler and A. Michaelides, *Phys. Rev. B: Condens. Matter Mater. Phys.*, 2011, **83**, 195131.
- 50 S. Nosé, *J. Chem. Phys.*, 1984, **81**, 511–519.
- 51 A. V. Kuklin, H. Ågren and P. V. Avramov, *Phys. Chem. Chem. Phys.*, 2020, **22**, 8289–8295.
- 52 S. Moon, S.-J. Chang, Y. Kim, O. F. N. Okello, J. Kim, J. Kim, H.-W. Jung, H.-K. Ahn, D.-S. Kim and S.-Y. Choi, *ACS Appl. Mater. Interfaces*, 2021, **13**, 59440–59449.
- 53 M. Yankowitz, Q. Ma, P. Jarillo-Herrero and B. J. LeRoy, *Nat. Rev. Phys.*, 2019, **1**, 112–125.
- 54 Q. Wang, J. Li, J. Lin and H. Jiang, *J. Appl. Phys.*, 2019, **125**, 205703.
- 55 K. D. Pham and C. V. Nguyen, *Diamond Relat. Mater.*, 2018, **88**, 151–157.
- 56 P. Lazić, *Comput. Phys. Commun.*, 2015, **197**, 324–334.
- 57 S. D. Chakarova-Käck, E. Schröder, B. I. Lundqvist and D. C. Langreth, *Phys. Rev. Lett.*, 2006, **96**, 146107.
- 58 H. K. Neupane and N. P. Adhikari, *AIP Adv.*, 2021, **11**, 085218.

